

Coherent terahertz microscopy of modal field distributions in micro-resonators

Cite as: APL Photonics 6, 066104 (2021); <https://doi.org/10.1063/5.0046186>

Submitted: 01 February 2021 . Accepted: 26 May 2021 . Published Online: 09 June 2021

Nikollao Sulollari,  James Keeley,  SaeJune Park,  Pierluigi Rubino,  Andrew D. Burnett,  Lianhe Li, Mark C. Rosamond,  Edmund H. Linfield,  A. Giles Davies,  John E. Cunningham, and  Paul Dean



View Online



Export Citation



CrossMark

ARTICLES YOU MAY BE INTERESTED IN

[Near-infrared nanospectroscopy using a low-noise supercontinuum source](#)

APL Photonics 6, 066106 (2021); <https://doi.org/10.1063/5.0050446>

[Optical constants from scattering-type scanning near-field optical microscope](#)

Applied Physics Letters 118, 041103 (2021); <https://doi.org/10.1063/5.0036872>

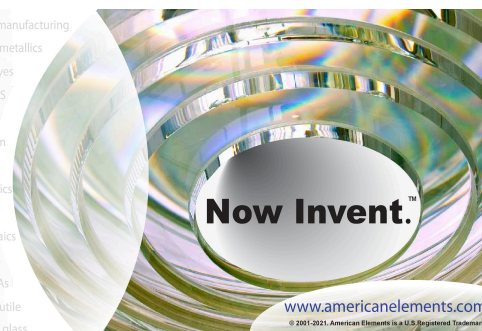
[Generation of half-integer harmonics and efficient THz-to-visible frequency conversion in strained graphene](#)

APL Photonics 6, 060801 (2021); <https://doi.org/10.1063/5.0049678>



yttrium iron garnet glassy carbon beamsplitters fused quartz additive manufacturing
 zeolites III-IV semiconductors gallium lump copper nanoparticles organometallics
 nano ribbons barium fluoride europium phosphors photonics infrared dyes
 epitaxial crystal growth ultra high purity materials transparent ceramics CIGS
 cerium oxide polishing powder cermet nanodispersions
 surface functionalized nanoparticles Al Si P S Cl Ar MRE grade materials thin film
 beta-barium borate OLED lighting solar energy
 rare earth metals quantum dots sputtering targets fiber optics
 osmium scintillation Ce:YAG h-BN deposition slugs
 refractory metals laser crystals CVD precursors photovoltaics
 anode lithium niobate InAs wafers metamaterials borosilicate glass
 dysprosium pellets MOFs AuNPs YBCO superconductors InGaAs
 chalcogenides ZnS CdTe indium tin oxide MgF2 rutile
 perovskite crystals transparent ceramics diamond micropowder optical glass

The Next Generation of Material Science Catalogs



Coherent terahertz microscopy of modal field distributions in micro-resonators

Cite as: APL Photon. 6, 066104 (2021); doi: 10.1063/5.0046186

Submitted: 1 February 2021 • Accepted: 26 May 2021 •

Published Online: 9 June 2021












View Online



Export Citation



CrossMark

Nikollao Sulollari,¹ James Keeley,¹  SaeJune Park,¹  Pierluigi Rubino,¹  Andrew D. Burnett,² 
Lianhe Li,¹  Mark C. Rosamond,¹ Edmund H. Linfield,¹  A. Giles Davies,¹  John E. Cunningham,¹ 
and Paul Dean^{1,a)} 

AFFILIATIONS

¹School of Electronic and Electrical Engineering, University of Leeds, Leeds LS2 9JT, United Kingdom

²School of Chemistry, University of Leeds, Leeds LS2 9JT, United Kingdom

^{a)} Author to whom correspondence should be addressed: p.dean@leeds.ac.uk

ABSTRACT

Near-field microscopy techniques operating in the terahertz (THz) frequency band offer the tantalizing possibility of visualizing with nanometric resolution the localized THz fields supported by individual resonators, micro-structured surfaces, and metamaterials. Such capabilities promise to underpin the future development and characterization of a wide range of devices, including THz emitters, detectors, optoelectronic modulators, sensors, and novel optical components. In this work, we report scattering-type scanning near-field optical microscopy using a THz-frequency quantum cascade laser (QCL) to probe coherently the localized field supported by individual micro-resonator structures. Our technique demonstrates deep sub-wavelength mapping of the field distribution associated with in-plane resonator modes in plasmonic dipole antennas and split ring resonator structures. By exploiting electronic tuning of the QCL in conjunction with the coherent self-mixing effect in these lasers, we are able to resolve both the magnitude and the phase of the out-of-plane field. We, furthermore, show that the elliptically polarized state of the QCL field can be exploited for the simultaneous excitation and measurement of plasmonic resonances in these structures while suppressing the otherwise dominant signal arising from the local material permittivity.

© 2021 Author(s). All article content, except where otherwise noted, is licensed under a Creative Commons Attribution (CC BY) license (<http://creativecommons.org/licenses/by/4.0/>). <https://doi.org/10.1063/5.0046186>

I. INTRODUCTION

Micro- and nano-scale resonators are essential components enabling a variety of technologies and devices operating in the terahertz (THz) frequency range, including THz detectors,^{1,2} sensors,³ and optoelectronic modulators.^{4–6} Individual resonators play a vital role in the strong subwavelength confinement of THz fields in such devices, thereby enhancing the interaction between light and matter, which may otherwise be weak owing to the relatively long wavelength of THz radiation. Sub-wavelength resonators are also important building blocks in the design of THz metamaterials and metasurfaces,^{7,8} underpinning a range of efficient and compact THz optoelectronic devices^{9–14} and enabling the development of novel optical elements, including magnetic mirrors,¹⁵ focusing elements,¹⁶ and negative refractive index materials.¹⁷ Among the wide variety of possible applications, metamaterials and structures based on subwavelength resonators have enabled THz sensing¹⁸ and

spectroscopy, where highly localized THz fields have made possible the detection of single micro-organisms;¹⁹ spectroscopic measurements of low-dimensional structures, including quantum dots;³ and the investigation of strong light–matter coupling in quantum heterostructures.^{20,21}

Owing to the small cross section of subwavelength resonators and single metamaterial elements, their interaction with diffraction-limited THz beams is typically weak. As such, the development and characterization of devices based on these structures most commonly rely on the measurement of the optical response of periodic or aperiodic arrays of nominally identical resonators in the far-field.^{1,3–6,12–15,17,19,21} However, such approaches are sensitive only to the ensemble-averaged optical properties of the array and can reveal only limited insights into the underlying light–matter interactions on the microscopic scale. In fact, these complex interactions can be strongly affected by radiative,²² capacitive,²³ or plasmonic²⁴ coupling between array elements, which can directly

influence the field confinement and spectral response of individual resonators, thus impeding the experimental investigation of their inherent electromagnetic properties. Furthermore, in addition to the well-known spectral broadening effects that afflict resonator arrays, significant spectral shifts have been observed when comparing the optical response of THz plasmonic nanoantennas and resonators measured in the near-field and far-field regimes^{25,26}—a phenomena attributed to the Fano interference of incident and scattered THz fields in the far-field.²⁷ In view of these considerations, it is becoming increasingly clear that the far-field characterization of sub-wavelength resonator arrays and associated metamaterials is insufficient to understand fully the complex interaction of THz waves with these structures.

To this end, there has been considerable interest in the application of near-field microscopy techniques for visualizing the localized THz fields supported by resonators and microstructured surfaces with sub-wavelength resolution. These include the use of miniaturized photoconductive,²⁸ electro-optic,^{29,30} or micrometer-scale aperture-based probes^{31,32} positioned directly in the near-field of the sample under investigation. However, in addition to the experimental complexity of these approaches and their reliance on bulky near-infrared fs lasers, they typically suffer from small signals and a poor dynamic range, meaning that the achievable spatial resolution is limited to the range of $\sim 1\text{--}30\ \mu\text{m}$. Furthermore, their reliance on THz generation schemes based on fs lasers limits the spectral range to frequencies below ~ 2 THz, thereby restricting the range of resonators and metamaterials that can be investigated. An alternative approach offering sub-micrometer spatial resolution has been adapted from apertureless (scattering-type) scanning near-field optical microscopy (s-SNOM).³³ This technique has been applied with great success to the mapping of localized fields and plasmonic effects at near-infrared and mid-infrared frequencies,^{34–38} with a nanometer-scale spatial resolution that is independent of the radiation wavelength. One notable recent innovation to the s-SNOM approach has been the use of a single quantum cascade laser (QCL) device as both the THz source and the coherent detector, through exploiting the self-mixing (SM) effect in these lasers.³⁹ In addition to the inherent advantages of QCL technology in terms of compact size, narrowband excitation with a spectral coverage over the range of $\sim 1\text{--}5.5$ THz, and relatively high output powers, the SM scheme offers remarkably low noise-equivalent powers at the $\sim \text{pW}/\sqrt{\text{Hz}}$ level,⁴⁰ it is therefore ideally suited to the detection of weak fields scattered from nanometer probes in THz-s-SNOM. This approach has recently been applied to the mapping of THz plasmonic resonances supported by photonic crystals and planar antennas, with a spatial resolution of $78\ \text{nm}$.⁴¹ However, this implementation permitted only visualization of the real component of the surface fields and could not resolve the field magnitude and phase separately. In fact, the mixing process between reinjected and intracavity fields in the laser SM scheme is inherently coherent, which has enabled the complex THz permittivity of samples to be probed in both near-field and far-field regimes.^{42,43}

In this work, we apply THz-s-SNOM using a THz QCL to map both the magnitude and the phase of the localized field spatially supported by individual micro-resonator structures. We show that the imperfect linear polarized state of the QCL field can, nonetheless, be exploited for the simultaneous excitation and measurement of plasmonic resonances in these structures while suppressing the

otherwise dominant signal arising from the local material permittivity. This new characterization technique opens the way for the future design and optimization of novel THz optoelectronic devices based on subwavelength resonators and associated metamaterials, as well as the nanoscale mapping of THz plasmons in emerging 2D materials and van der Waals heterostructures.^{44,45}

II. RESULTS AND DISCUSSION

A. THz-s-SNOM system

Our THz-s-SNOM instrument is based on a commercial s-SNOM/AFM platform (neaSNOM, neaspec GmbH) but incorporates an external THz QCL source emitting at $\nu \sim 3.45$ THz (see the Appendix). Radiation emitted from the laser was collected and focused to the $\sim 20\ \text{nm}$ apex of the near-field microscope probe, which was positioned in the near-field of the sample surface, as shown in Fig. 1(a). Under excitation from a p-polarized beam, radiation is strongly confined at the nanoscale tip apex. The resulting interaction between the probe tip and the sample surface causes a near-field enhancement of the scattering cross section of the tip-sample system that depends on the local sample permittivity. This mechanism has been described previously using various numeric and analytic theoretical frameworks, including point dipole,^{46,47} finite dipole,⁴⁸ and electrodynamic lightning rod models.⁴⁹

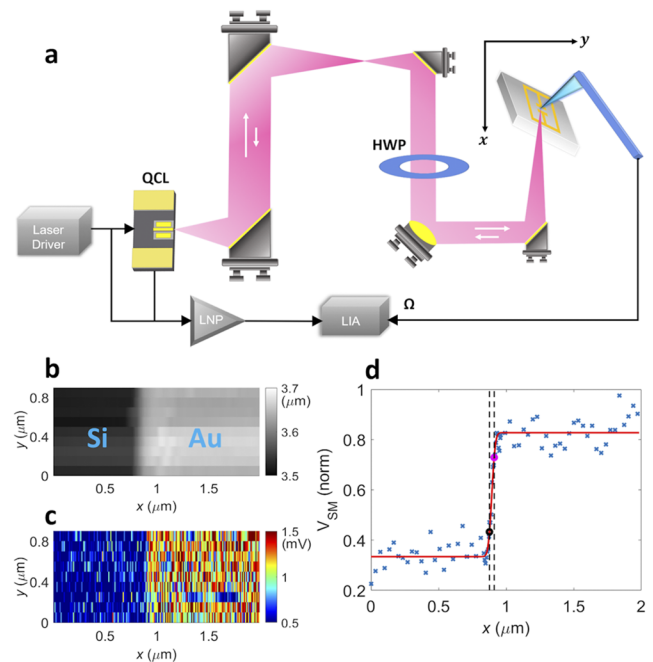


FIG. 1. (a) Experimental diagram of the THz-s-SNOM system in which radiation from a THz QCL is coupled to and from the tip of an AFM probe. LIA: Lock-in amplifier and LNP: Low-noise preamplifier. (b) AFM image and (c) THz-s-SNOM image of a gold-on-silicon resolution target. The scan area of each image is $2 \times 1\ \mu\text{m}^2$ with a $10\ \text{nm}$ step size in the x direction and $100\ \text{nm}$ step size in the y direction. The tapping amplitude was $30\ \text{nm}$. (d) The ERF determined from the voltage signals extracted along the x direction of (c), yielding a spatial resolution of $35\ \text{nm}$. Blue dots: experimental data. Red line: fitted ERF.

In our system, the radiation scattered to the far-field by the probe is coupled back to the QCL along the same optical path as the incident beam and reinjected to the laser cavity. The resulting mixing process between the intracavity and reinjected fields generates a perturbation to the laser voltage, via the laser SM effect, that is proportional to the reinjected field. This detection approach provides a high detection sensitivity while removing the need for both an external detector and an external interferometer to resolve the scattered field coherently.⁵⁰ To isolate the signal component arising from the near-field interaction between the probe and the sample, the microscope probe was operating in a tapping mode and the QCL terminal voltage was demodulated at harmonics of the tip tapping frequency ($\Omega \sim 80$ kHz) using a lock-in amplifier. By raster-scanning the sample in two dimensions, images with deep sub-wavelength resolution could, thereby, be obtained up to the $n = 5$ signal harmonic.

To quantify the spatial resolution of our THz-s-SNOM instrument, two-dimensional images were acquired using a resolution target comprising 50-nm-thick gold stripes patterned on a silicon substrate using electron-beam lithography. Figures 1(b) and 1(c) show, respectively, the sample topography recorded by AFM and the corresponding THz near-field image obtained from the $n = 3$ harmonic signal. By averaging the signal measured from ten adjacent rows of pixels, the edge response function (ERF) shown in Fig. 1(d) is obtained. Applying the 20%–80% criterion to the ERF yields a spatial resolution of 35 nm, corresponding to a subwavelength resolution of $\sim \lambda/2, 500$. It should be noted that this resolution depends principally on the tip apex size and the tapping amplitude and could, in principle, be further reduced at the expense of signal size through the use of a sharper tip and smaller amplitude. It should also be noted that this measured value of resolution may be influenced by the topography of our resolution target, which is known to introduce topography-induced contrast, as well as by screening effects in the metallic layer.^{51–53}

B. Sample design, fabrication, and characterization

Coherent mapping of the localized field distribution supported by individual micro-resonators was demonstrated using two exemplary structures. The first consisted of a simple dipole antenna structure that was engineered to support a plasmonic resonance at the excitation frequency ν_{res} of ~ 3.45 THz. The dipole antenna can be described as a quasi-one-dimensional Fabry-Pérot resonator of length L given by

$$L = \frac{m\lambda_p}{2} = \frac{mc}{2n_{eff}\nu_{res}}, \quad (1)$$

where λ_p is the plasmon wavelength, c is the speed of light, and n_{eff} is the effective refractive index of the plasmonic mode. Figure S1 shows the simulated S_{21} parameter for a 100-nm-thick gold structure with dimensions $15 \times 2 \mu\text{m}^2$ (see the Appendix). A sharp first-order ($m = 1$) resonance is observed at $\nu_{res} = 3.45$ THz, indicating a plasmon wavelength of $\lambda_p = 30 \mu\text{m}$ and a value of $n_{eff} = 2.9$ obtained from Eq. (1). To visualize this plasmonic mode driven by the incoming wave, the magnitude and phase of the out-of-plane electric field component E_z were calculated in the x - y plane at a distance of 20 nm above the sample surface. As shown in Figs. 2(a) and 2(b), the field is strongly enhanced at both ends of the structure, with a π radian phase difference between the two ends.

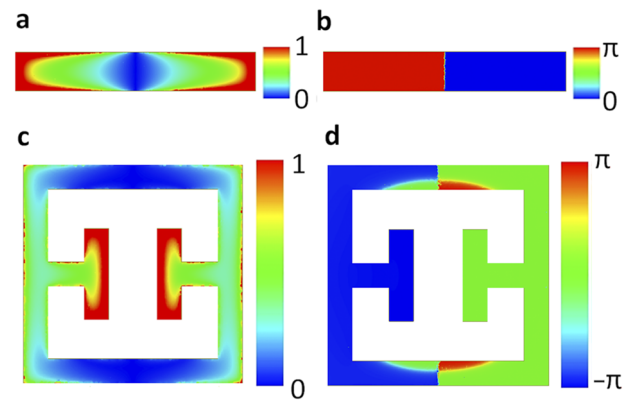


FIG. 2. Simulated (a) magnitude and (b) phase of the out-of-plane field measured in the x - y plane 20 nm above a dipole antenna structure with dimensions $15 \times 2 \mu\text{m}^2$. The structures are illuminated at normal incidence with an x -polarized plane wave with frequency 3.45 THz. (c) Magnitude and (d) phase maps for a split ring resonator (SRR) structure with dimensions $9 \times 9 \mu\text{m}^2$ for the same excitation conditions. The color scales in (a) and (c) are normalized to the maximum field magnitude in each case.

The second structure investigated was a THz metamaterial consisting of a periodic array of split ring resonators (SRRs). Each SRR supports an inductive-capacitive resonance, whereby surface current modes are strongly excited by interaction with the incident field. Figure S1 shows the simulated S_{21} parameter for a $9 \times 9 \mu\text{m}^2$ structure with a gap width of $2 \mu\text{m}$ and a periodicity of $12.5 \mu\text{m}$ ($\approx \lambda_{res}/7$). The magnitude and phase of E_z at the resonant frequency $\nu_{res} \sim 3.45$ THz are shown in Figs. 2(c) and 2(d), respectively. In this case, the electric field is strongly enhanced at the edges of the capacitive gap and the field oscillates in these regions with a 0 or π radian phase difference with respect to the incident field.

Figures 3(a) and 3(b) show AFM images of periodic arrays of each resonator structure fabricated in gold on a silicon substrate (see the Appendix). The transmission parameters measured by THz time-domain spectroscopy (see the Appendix) are shown in Fig. 3(c). In each case, a clear resonance is observed at the design frequency when the polarization of the incident beam is aligned in the horizontal (x) direction. The weaker and broader resonances observed experimentally, when compared to the simulations, can be attributed to limitations in the spatial resolution of the lithographic technique and lift-off process used during fabrication, as well as losses in the metallic layers of experimental devices.

C. THz-s-SNOM of microscale resonators

In the case of samples as shown in Fig. 1, which do not support resonant modes at the radiation frequency, image contrast arises solely from the spatial variation of the local dielectric properties of the sample in the near-field of the tip. To engage this, imaging mode efficiently requires a p-polarized excitation beam, for which the interaction with the vertically aligned probe is significantly stronger than for s-polarized radiation.⁴⁷ In the case of resonant samples, however, in-plane modes may be excited directly using s-polarized radiation of the appropriate frequency. Any out-of-plane (z direction) fields supported by the excited resonant sample will then be

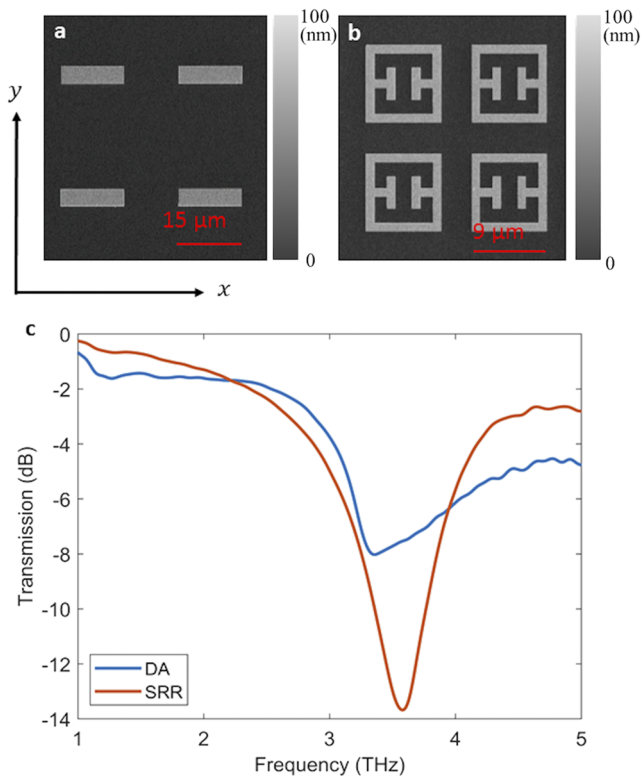


FIG. 3. AFM images of fabricated arrays of (a) dipole antenna (DA, blue line) and (b) split ring resonator (SRR, red line) structures. (c) THz transmission properties of the fabricated arrays obtained using THz-TDS, each showing a resonance close to the design frequency of ~ 3.45 THz.

scattered strongly to the far-field, whereas in-plane field components will scatter only weakly from the vertically aligned probe. In the more general case of a resonant sample illuminated by an incident beam of arbitrary polarization, the predominantly p-polarized field scattered to the far-field can therefore be expressed as

$$E_{\text{scat}} = \sigma_{\varepsilon} E_{\perp} + \sigma_z E_z. \quad (2)$$

Here, E_{\perp} represents the out-of-plane component of the incident field and σ_{ε} is the complex scattering efficiency that encapsulates the near-field dipole interaction between the illuminated tip and the sample surface.⁵⁴ E_z represents the out-of-plane field component associated with resonant modes supported by the sample, which can be excited by appropriately oriented in-plane components of the incident field E_{\parallel} , and the complex parameter σ_z quantifies the efficiency with which E_z is scattered to the far-field.

In our experiment, radiation scattered by the probe to the far-field is typically weak, and the laser is therefore operated in the regime of weak optical feedback.⁵⁵ Under these conditions, the measured SM voltage signal V_{SM} is proportional to the scattered field that is reinjected to the laser cavity after accumulating a round-trip phase $\phi_L = 4\pi L_{\text{ext}} \nu / c$ in the external cavity of length L_{ext} formed between the laser facet and the probe tip.⁵⁶ A variation in the round-trip phase, accomplished through either mechanical extension of the

external cavity or electronic control of the laser frequency, thereby induces a series of interferometric fringes in the demodulated SM voltage signal, the complex amplitude of which relates directly to the scattered field E_{scat} . Following Eq. (2), the SM signal can be expressed in terms of magnitudes, s_{ε} and s_z , and phases, ϕ_{ε} and ϕ_z , of the individual signal contributions corresponding to the respective scattering terms according to

$$V_{SM} = (s_{\varepsilon} e^{-i\phi_{\varepsilon}} + s_z e^{-i\phi_z}) e^{i\phi_L}. \quad (3)$$

Here, the magnitudes s_{ε} and s_z encapsulate several factors, including the respective excitation field strengths, the feedback parameter (itself accounting for the reinjection efficiency to the laser cavity), and the optoelectronic response of the laser active region. We can, furthermore, note that the phase $\phi_{\varepsilon} \approx 0$ for radiation frequencies far away from any phonon or bulk plasmonic material resonances.⁴³ This also permits the round-trip phase $\phi_L = 2\pi m$ to be set experimentally, through a fine adjustment of the external cavity length, by maximizing the signal measured from a region of the sample where no out-of-plane field exists (i.e., for which $s_z = 0$). The SM voltage signal then simplifies to

$$V_{SM} = s_{\varepsilon} + s_z e^{-i\phi_z}. \quad (4)$$

Hence, the s-SNOM signal may comprise two contributions: the first, s_{ε} , is principally excited by p-polarized components of the incident radiation and captures information on the local permittivity of the sample. The second is excited by in-plane components of the incident field and is insensitive to the bulk material properties but captures the spatial distribution of the out-of-plane field supported by the sample under resonant excitation. The relative contributions of these two terms can be controlled through either control of the polarization state of the incident field or through the variation of the sample orientation with respect to this field.

In our system, the epitaxial growth direction of the QCL heterostructure stack is aligned parallel to the probe axis (z direction). Owing to the selection rules for intersubband transitions in QCLs, which dictate the emission of predominantly transverse magnetic (TM) polarized modes, the excitation field is therefore predominantly p-polarized with an in-plane component along the x direction. Figures 4(a) and 4(c) show, respectively, THz near-field images of the dipole antenna structure and SRR structure each with their principal axis orientated along this direction. For comparison, THz images of both structures when orientated along the orthogonal (y) direction are shown in Figs. 4(b) and 4(d). The noise in these images can be attributed to several sources, including surface roughness of the metallic layers, mechanical vibration, thermal drift of the QCL operating temperature, and laser voltage noise. Figures 4(e)–4(h) show the corresponding spatial maps of E_z obtained from finite-element method (FEM) simulations of each structure assuming a p-polarized excitation beam. Excellent agreement between experimental and simulated images is obtained, albeit with the experimentally measured signals being offset by a constant (spatially homogeneous) positive voltage across the structure (see below). In particular, the THz image reveals clear signal contrast between opposite ends of the dipole structure when the resonator axis is aligned along the x direction [“on resonance” orientation; Fig. 4(a)]. These features, which do not appear for the orthogonal

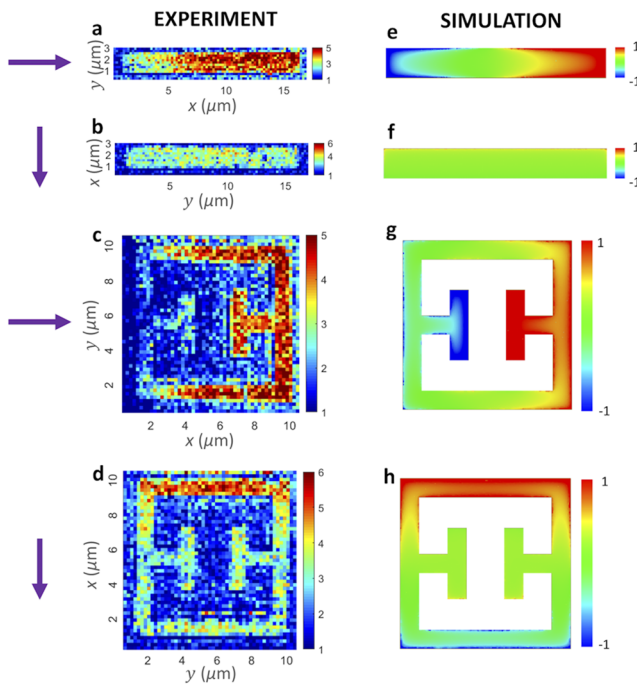


FIG. 4. THz-s-SNOM images of the individual [(a) and (b)] dipole antenna and [(c) and (d)] SRR structures measured at the resonant frequency of ~ 3.45 THz. The color scale represents the measured SM voltage signal, described by the real part of Eq. (4). The arrows indicate the in-plane polarization of the excitation field; in (a) and (c), the field is orientated to excite a resonance in each structure (“on resonance” orientation), whereas in (b) and (d), no resonance is excited (“off resonance” orientation). [(e)–(h)] Corresponding simulations of the out-of-plane field in the x – y plane 20 nm above the sample surface.

sample orientation [“off resonance,” Fig. 4(b)], are a clear indication of a dipolar plasmonic mode being excited in the structure and subsequently probed in the near-field using our approach.

A strong in-plane resonant mode, characterized by opposing surface fields supported at the edges of the capacitive gap, is similarly revealed in the THz image of the SRR structure only when orientated appropriately with respect to the incident field [“on resonance” orientation; Fig. 4(c)]. In the “off resonance” orientation [Fig. 4(d)], this mode is not excited although a larger voltage signal is recorded along one edge of the structure. This feature, which is also predicted through simulation of the out-of-plane field distribution [Fig. 4(h)], can be attributed to a mode excited in the outer ring of the SRR with the asymmetry arising from the oblique illumination geometry. This oblique illumination, which causes the phase of the excitation field to vary linearly along the x direction, will also give rise to a spatial variation in the phase of the scattered field as the spatially structured sample is scanned within the beam. This phenomenon is expected to manifest in all the recorded images shown in Fig. 4, although its effect may be obscured by the field distribution of the sample’s resonant mode or may be negligible when the sample is spatially small along the y dimension. Further differences between measured and simulated results in Fig. 4 may arise from shadowing effects or through coupling of the tip and resonator, altering the resonant

properties of the resonators. This latter effect would be dependent on both the geometry and dielectric properties of the tip.

D. Microscopy of plasmonic modes using s-polarized excitation

Although experimentally convenient, the images shown in Fig. 4 highlight two limitations of employing a p-polarized excitation beam for mapping resonant modes in such structures. First, the generation of field components necessary for the excitation of in-plane modes unavoidably results in a component of beam propagation along the principal axis of the resonator. The recorded images are thereby susceptible to phase retardation effects that can obscure the spatial distribution of the out-of-plane field supported by the sample. Second, a p-polarized beam is extremely efficient at exciting a near-field interaction between the illuminated tip and the sample surface, giving rise to a strong signal component, s_e , that depends only on the local material properties of the sample. On the other hand, an s-polarized excitation beam may be employed to excite in-plane resonant modes selectively while mitigating against phase retardation effects along the resonator axis. To that end, we have employed a quartz zero-order half-wave plate (HWP), positioned in the beam path between the QCL and the near-field probe, to control the incident polarization state in our system. By aligning the fast axis at $\theta_{WP} = 45^\circ$ to the z direction, a predominantly s-polarized excitation beam can be generated. At the same time, this results in the p-polarized field scattered by the probe also being rotated such that the field reinjected to the QCL cavity becomes polarized *perpendicular* to the growth direction of the heterostructure. It is expected that such field components would not mix efficiently with the orthogonally polarized intracavity laser field and would therefore not generate a measurable SM voltage signal. Nevertheless, a full characterization of the polarization properties of the THz beam emitted by our QCL has revealed a small but non-negligible component of circularly polarized light (see the Appendix). The occurrence of a non-pure TM polarization has similarly been observed in mid-infrared QCLs, where it has been attributed to residual birefringence present in the QCL waveguide, resulting in a conversion of linear polarization into a circular polarization.^{57,58} In this way, and as is demonstrated experimentally below, the linearly polarized reinjected field may mix with a non-negligible component of the QCL field, generating a small but measurable voltage perturbation via the SM effect.

To demonstrate the near-field mapping of in-plane resonant modes under s-polarized excitation, THz near-field images were recorded for different orientations of the HWP. Figure 5 shows a series of images acquired for the dipole structure orientated with its axis along the y direction for wave plate angles in the range of $\theta_{WP} = 0^\circ$ – 45° . In each image, the measured signal is expected to follow Eq. (3) in which the relative size of the two terms is determined by the incident field components E_\perp and E_\parallel , which, in turn, are controlled through θ_{WP} . With $\theta_{WP} = 0^\circ$, the incident field is p-polarized and $s_z = 0$. As such, this image captures only the local permittivity of the sample, which is spatially homogeneous within the metallic regions [see Fig. 5(a)]. Conversely, with $\theta_{WP} = 45^\circ$, the term s_e is small and the image predominantly captures the out-of-plane field component associated with the plasmonic mode supported by the sample, E_z [see Fig. 5(f)]. Our approach is therefore seen to be

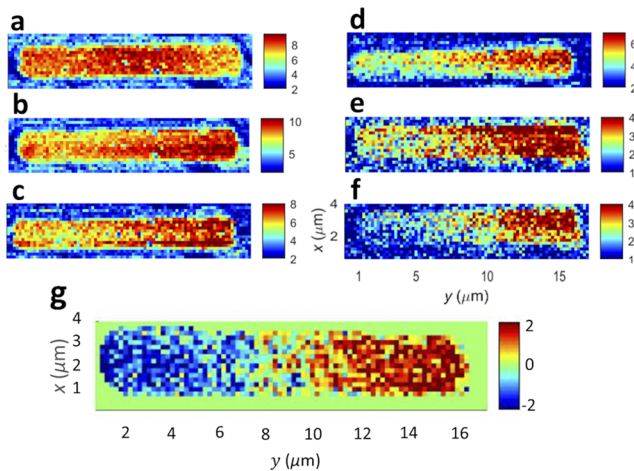


FIG. 5. THz-s-SNOM images of an individual dipole antenna structure orientated with its axis along the y direction, acquired with the fast axis of the half-wave plate orientated at angles (a) $\theta_{WHP} = 0^\circ$ (p-polarized), (b) 20° , (c) 30° , (d) 35° , (e) 40° , and (f) 45° (s-polarized) relative to the z direction. (g) Post-processed THz-s-SNOM image acquired with an s-polarized excitation beam, revealing only the out-of-plane field distribution supported by the sample under resonant excitation. The spatially homogeneous signal arising from the dipole interaction between the tip and the sample has been subtracted from the image. To improve visibility of the image features, the corresponding AFM image has been used as a mask to null the substrate signal outside the borders of the dipole antenna.

effective in selectively exciting plasmonic modes in the sample while mitigating against retardation effects and, by virtue of the elliptically polarized QCL field, retains the capability of sensing the p-polarized radiation scattered to the far-field.

Further quantitative analysis of these images (see [supplementary material](#), Fig. S2) reveals a signal component s_ε that persists even for an HWP angle $\theta_{WHP} = 45^\circ$. This can be attributed to a combination of factors that cause the origin of the measured signals to deviate from the simplified description given above. First, the elliptically polarized QCL field has the effect of exciting the sample with non-vanishing p- and s-polarized field components irrespective of the wave plate orientation. This effect is further compounded by the imperfect nature of the HWP retardation, which acts to accentuate the polarization ellipticity in both the incident and reinjected fields. Nevertheless, we note that the field distribution associated with the in-plane plasmonic mode exhibits equal magnitude but opposite phase in opposite halves of the structure [i.e., $s_z e^{-i\phi_z}$ is spatially asymmetric; see, for example, [Figs. 2\(a\)](#), [2\(b\)](#), and [4\(e\)](#)] and will therefore spatially average to zero. As such, the signal component s_ε can be readily estimated from the spatial average of the signal recorded across all gold regions of the sample. Subtraction of this component from each pixel in the image then retains only a measurement of the out-of-plane field distribution supported by the sample under resonant excitation. The result of this post-processing is shown in [Fig. 5\(g\)](#) and shows excellent agreement with simulations.

It should be noted that the spatial resolution determined from [Fig. 1\(d\)](#) for imaging dielectric contrast in samples is not replicated when imaging out-of-plane field distributions, as shown in [Fig. 5\(g\)](#).

This possibility arises first from the distinct physical mechanisms, giving rise to these two signal components, which may influence the spatial variation of the measured signal differently, particularly at sample edges and near material boundaries.^{52,53,59} Furthermore, typically weaker THz field enhancements are supported by resonator structures under s-polarized excitation compared to at the apex of the scattering tip under p-polarized excitation. This results in a smaller signal-to-noise ratio (SNR) when imaging the out-of-plane field distributions, which may, in turn, limit the practical spatial resolution of these measurements. Nevertheless, our measurements provide some insight into the relative size of this signal. From [Fig. 5\(a\)](#), we obtain a signal magnitude of $s_\varepsilon \sim 7.8$ mV arising from the local sample permittivity with p-polarized excitation. This is compared to a maximum signal magnitude of $s_z \sim 1.5$ mV obtained with s-polarized excitation from [Fig. 5\(g\)](#). Although slightly smaller, this value suggests that an adequate SNR is retained, sufficient for deep sub-wavelength mapping of the field distributions associated with in-plane resonator modes. This is also borne out by the quality of the images obtained in [Figs. 4](#) and [5](#). However, further measurements would be required to obtain a quantitative estimate of this spatial resolution. For this purpose, resonator structures supporting modes that are both well-defined spatially and are confined on sub-micron scales would be desirable.

E. Coherent THz-s-SNOM of microscale resonators

The coherent mixing process between reinjected and laser cavity fields in the SM scheme offers the possibility of electronically capturing both the magnitude and the phase of the scattered field, E_{scat} . We achieve this using a measurement approach adapted from coherent far-field THz imaging⁴² and recently applied to the coherent microscopy of a phonon-polariton-resonant crystal⁶⁰ (see the [supplementary material](#)). In addition to offering reduced experimental complexity compared to alternative approaches based on the mechanical extension of the optical beam path,⁴³ electronic modulation schemes have been demonstrated to enable faster acquisition in far-field THz imaging and also to improve phase stability significantly owing to the associated reduction in the slow thermal drift of the QCL emission frequency.⁶¹

For these coherent measurements, a series of images were acquired with the lasing frequency being tuned electronically by ~ 100 MHz between successive raster scans of the sample (see the [Appendix](#)). For each image pixel, a series of interferometric fringes in the n -th harmonic of the demodulated SM voltage signal was thereby obtained. The magnitude of the complex amplitude of the fringes can then be calculated on a pixel-by-pixel basis as $s_n = |\mathcal{F}(\tau)|$ and the phase as $\phi_n = \arctan\{\Im[\mathcal{F}(\tau)]/\Re[\mathcal{F}(\tau)]\}$, in which $\mathcal{F}(\tau)$ is the complex Fourier transform of the voltage signal evaluated at the fundamental fringe periodicity (see the [supplementary material](#)).⁶¹ [Figures 6\(a\)](#) and [6\(b\)](#) show the magnitude and phase determined in this way and spatially averaged across three adjacent rows of pixels spanning the long axis of the dipole structure. Similarly to the images shown in [Fig. 5](#), a non-negligible signal component arising from the dipole interaction between the tip and the dielectric sample is evident, which can be quantified from the spatial average of the complex amplitude recorded across all gold regions of the sample, as described previously. Finally, the magnitude s_z and phase ϕ_z of the signal component associated with the plasmonic mode can be

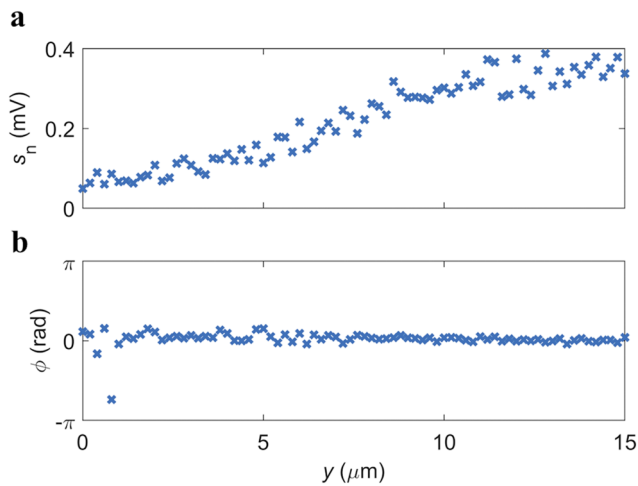


FIG. 6. (a) Magnitude and (b) phase of the SM voltage interferograms obtained from coherent THz-s-SNOM measurements along the long axis (y direction) of an individual dipole antenna. The step size is 200 nm.

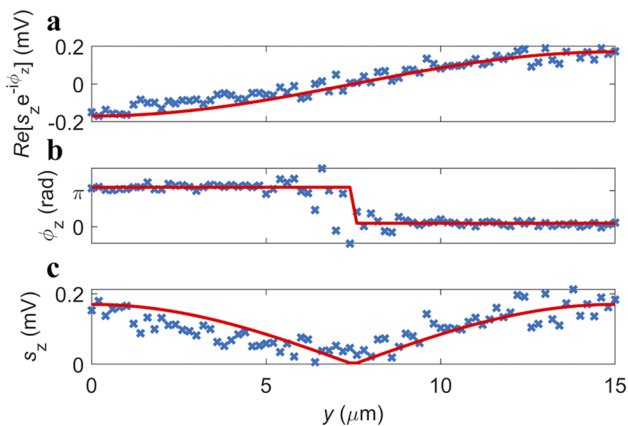


FIG. 7. (a) Real part $\Re[s_z e^{-i\phi_z}]$, (b) phase ϕ_z , and (c) magnitude s_z of the signal component corresponding to the out-of-plane field associated with the plasmonic mode excited in the dipole antenna structure. Blue dots: experimental data obtained from coherent THz-s-SNOM measurements along the long axis (y direction) of the resonator. Red line: corresponding real part, phase, and magnitude values for the out-of-plane field obtained from simulations.

isolated for each pixel in the image (see the [supplementary material](#)). The results of this analysis are shown in [Fig. 7](#). For comparison, the magnitude and phase of the out-of-plane electric field component E_z associated with the plasmonic mode, calculated from FEM simulations, are also shown. Excellent agreement is obtained between measurement and simulation, with the principal characteristics of the first-order dipolar plasmonic mode being faithfully captured by our coherent near-field measurement approach.

III. CONCLUSION

In summary, we have demonstrated coherent THz near-field microscopy using a QCL as both the THz source and the coherent detector. Our approach provides a deep sub-wavelength spatial

resolution of ~ 35 nm, enabling the high-resolution imaging of individual micro-resonator structures at frequencies beyond the typical ~ 2 THz bandwidth of pulsed THz systems. Through control of the polarization state of the excitation beam, we have demonstrated the selective excitation and spatial mapping of in-plane resonant modes supported by SRR and plasmonic dipole antenna structures while suppressing phase retardation effects and reducing the otherwise dominant signal arising from the local material permittivity. Central to this scheme is the imperfectly linear polarized state of the QCL field, which can be exploited to enable sensitive detection of the field scattered from the s-SNOM tip through the SM effect in these lasers. Furthermore, we have developed a coherent measurement approach, adapted from coherent far-field THz imaging, to simultaneously resolve both the magnitude and the phase of the scattered field. This approach has been applied, for the first time, to the spatial and coherent mapping of the out-of-plane field associated with THz plasmonic resonances, showing accurate agreement with FEM simulations of these plasmonic modes. We envisage that our new coherent THz near-field imaging technique will open the way for the future design and optimization of novel THz optoelectronic devices and sensors based on subwavelength resonators and associated metamaterials, as well as the nanoscale mapping of THz plasmons and phonon polaritons in emerging 2D materials.

SUPPLEMENTARY MATERIAL

See the [supplementary material](#) for the supporting content.

AUTHORS' CONTRIBUTIONS

P.D., N.S., and J.K. conceived the idea, developed the experimental setup, and performed the measurements. Resonator structures were designed by N.S. and S.P. and fabricated by N.S. under the supervision of M.C.R. Data were analyzed by N.S. and J.K. with support from P.D., J.E.C., S.P., and A.D.B. The QCL structure was grown by L.L. under the supervision of E.H.L. Devices were processed by P.R. under the supervision of E.H.L. and A.G.D. The manuscript was written by N.S., P.D., S.P., A.D.B., and J.E.C. with contributions from all the authors.

ACKNOWLEDGMENTS

The authors acknowledge support from the EPSRC Programme Grant “HyperTerahertz” (No. EP/P021859/1) and the EPSRC, Grant No. EP/R00501X/1. A.D.B. acknowledges support from his EPSRC fellowship (No. EP/P007449/1). E.H.L. acknowledges support from the Royal Society and the Wolfson Foundation.

APPENDIX: METHODS

1. Simulation

Finite-element method (FEM) simulations of the resonator structures were performed using Ansys HFSS software. Metallic regions were treated as a perfect electrical conductor with thickness 100 nm defined on a $50 \mu\text{m}$ silicon substrate with permittivity 11.65, determined experimentally from THz time-domain spectroscopy

(THz-TDS) measurements. The structure was illuminated by a linearly polarized plane wave under either normal illumination (in the case of Fig. 2) or with an angle of incidence of 54° (in the case of Fig. 4), to reproduce the experimental conditions in the s-SNOM system. Periodic boundary conditions were defined at the edges of the simulation volume with a periodicity of $12.5\ \mu\text{m}$ for the SRRs and $13\ \mu\text{m}$ spacing between the dipole resonators. Wave ports positioned $250\ \mu\text{m}$ apart and lying in the x - y planes above and below the structure were used to obtain S_{21} parameters (see Fig. S1). Based on these simulated parameters, both the dipole antenna and SRR structures exhibit a resonance at $\sim 3.45\ \text{THz}$, with Q factors of 69 and 39, respectively. The spatial distributions of the out-of-plane electric field E_z associated with the resonant modes were calculated in the x - y plane $20\ \text{nm}$ above the structure.

2. Sample fabrication

Structures were fabricated using standard electron-beam lithography on a high resistivity ($>10\ 000\ \Omega\ \text{cm}$) undoped silicon substrate with a thickness of $525 \pm 25\ \mu\text{m}$. The thickness of the Ti/Au resonators was $\sim 2\ \text{nm}/\sim 100\ \text{nm}$. Structures were patterned across a $2 \times 2\ \text{mm}^2$ region with a periodicity of $12.5\ \mu\text{m}$ for the SRRs and a spacing of $13\ \mu\text{m}$ between the dipole resonators.

3. Time-domain spectroscopy

The THz-TDS system used has been described in detail elsewhere.⁶² In brief, a $800\ \text{nm}$ wavelength mode-locked Ti:sapphire laser (Vitara, Coherent) providing pulses with a width of $20\ \text{fs}$ at an $80\ \text{MHz}$ repetition rate was used to generate THz pulses from a photoconductive (PC) emitter comprising a 300-nm -thick piece of low-temperature grown GaAs (LT-GaAs) bonded onto a 5-mm -thick quartz substrate.⁶² Detection was achieved using a time-delayed probe beam derived from the fs laser to excite an identical second PC device. All data shown were collected in a nitrogen environment to remove the effect of water absorption in atmosphere.

4. THz-s-SNOM system

The light source used was a single-mode THz QCL consisting of a $14\text{-}\mu\text{m}$ -thick GaAs/AlGaAs nine-well hybrid active region lasing at $\sim 3.45\ \text{THz}$, which was processed into a semi-insulating surface-plasmon ridge waveguide with dimensions of $1.8\ \text{mm} \times 150\ \mu\text{m}$. The QCL was cooled using a continuous-flow L-He cryostat and maintained at a heat sink temperature of $20 \pm 0.01\ \text{K}$. A current source was used to drive the laser with a dc current of $420\ \text{mA}$, just above the lasing threshold current of $\sim 400\ \text{mA}$. At this driving current, the QCL voltage was $6.4\ \text{V}$ and the emitted power was $\sim 1\ \text{mW}$. Emission from the QCL was focused to the vertically aligned tip of the s-SNOM system at an angle of $\sim 54^\circ$ relative to the surface normal, and the length of the external cavity formed between the tip and the QCL facet was $L_0 = 60\ \text{cm}$. A quartz zero-order half-wave plate, positioned in the beam path between the QCL and the s-SNOM tip, was used to control the polarization state of the beam incident on the sample. The self-mixing signal, arising from the field scattered from the s-SNOM tip and reinjected to the laser cavity, was derived from the $n = 3$ harmonic of the demodulated QCL terminal voltage after amplification using an ac-coupled low-noise voltage amplifier.

Single-frequency THz-s-SNOM images of resonator structures were acquired with a step size of $200\ \text{nm}$, a tip tapping amplitude of $\sim 175\ \text{nm}$, and an integration time of $200\ \text{ms}$. For coherent THz-s-SNOM measurements, successive images were acquired with the QCL driving current being stepped incrementally in the range of $598\text{--}704\ \text{mA}$. Over this operating range, the QCL emits on a single longitudinal cavity mode that tunes over a frequency range of $\sim 900\ \text{MHz}$, corresponding to approximately three interferometric fringes in the SM voltage signal.

5. Measurement of QCL polarization

The Stokes parameters of the QCL were measured using the standard method described elsewhere.⁵⁷ Briefly, the THz beam was propagated through a quartz zero-order quarter-wave plate and wire grid linear polarizer and detected using a helium-cooled germanium bolometer. The QCL was driven with a dc current with a mechanical chopper used to modulate the THz beam at a frequency of $80\ \text{Hz}$ for lock-in detection of the detector signal. With a laser drive current of $420\ \text{mA}$, the normalized Stokes parameters were determined to be $S_1 = 0.96$, $S_2 = 0$, and $S_3 = 0.27$, with a degree of polarization, $P = 1$. Measurements performed at higher currents up to $700\ \text{mA}$ yielded similar results (see the supplementary material), confirming that the polarization state is not significantly affected by driving conditions. From these values, the QCL emission is seen to contain a non-negligible degree of right circularly polarized light, yielding a polarization ellipse with orientation angle $\psi = 0^\circ$ (orientated parallel to the QCL growth direction) and ellipticity angle $\chi = 8^\circ$. The elliptically polarized emission was further confirmed through measurement of the Jones vector using a pair of identical wire grid polarizers.⁶³ This analysis yielded an ellipticity coefficient factor of $R = 0.18$, indicating an ellipticity angle $\chi = 10^\circ$ in good agreement with that obtained from the Stokes parameters.

DATA AVAILABILITY

The data utilized in the development of this article can be found at: URL: <https://doi.org/10.5518/989>.

REFERENCES

- 1C. Belacel *et al.*, "Optomechanical terahertz detection with single meta-atom resonator," *Nat. Commun.* **8**, 1578 (2017).
- 2R. Degl'Innocenti *et al.*, "Fast room-temperature detection of terahertz quantum cascade lasers with graphene-loaded bow-tie plasmonic antenna arrays," *ACS Photonics* **3**, 1747–1753 (2016).
- 3A. Toma, "Squeezing terahertz light into nanovolumes: Nanoantenna enhanced terahertz spectroscopy (NETS) of semiconductor quantum dots," *Nano Lett.* **15**, 386–391 (2015).
- 4R. Degl'Innocenti *et al.*, "Low-bias terahertz amplitude modulator based on splitting resonators and graphene," *ACS Nano* **8**, 2548–2554 (2014).
- 5R. Degl'Innocenti *et al.*, "Fast modulation of terahertz quantum cascade lasers using graphene loaded plasmonic antennas," *ACS Photonics* **3**, 464–470 (2016).
- 6B. Wei *et al.*, "Amplitude stabilization and active control of a terahertz quantum cascade laser with a graphene loaded split-ring-resonator array," *Appl. Phys. Lett.* **112**, 201102 (2018).
- 7N. Meinzer, W. L. Barnes, and I. R. Hooper, "Plasmonic meta-atoms and metasurfaces," *Nat. Photonics* **8**, 889–898 (2014).
- 8J. Shi *et al.*, "THz photonics in two dimensional materials and metamaterials: Properties, devices and prospects," *J. Mater. Chem. C* **6**, 1291–1306 (2018).

- ⁹S. Keren-Zur, M. Tal, S. Fleischer, D. M. Mittleman, and T. Ellenbogen, "Generation of spatiotemporally tailored terahertz wavepackets by nonlinear metasurfaces," *Nat. Commun.* **10**, 1778 (2019).
- ¹⁰L. Luo *et al.*, "Broadband terahertz generation from metamaterials," *Nat. Commun.* **5**, 3055 (2014).
- ¹¹T. Siday *et al.*, "Terahertz detection with perfectly-absorbing photoconductive metasurface," *Nano Lett.* **19**, 2888–2896 (2019).
- ¹²S. H. Lee *et al.*, "Switching terahertz waves with gate-controlled active graphene metamaterials," *Nat. Mater.* **11**, 936–941 (2012).
- ¹³F. Valmorra *et al.*, "Low-bias active control of terahertz waves by coupling large-area CVD graphene to a terahertz metamaterial," *Nano Lett.* **13**, 3193–3198 (2013).
- ¹⁴H.-T. Chen *et al.*, "Experimental demonstration of frequency-agile terahertz metamaterials," *Nat. Photonics* **2**, 295–298 (2008).
- ¹⁵Z. Ma *et al.*, "Terahertz all-dielectric magnetic mirror metasurfaces," *ACS Photonics* **3**, 1010–1018 (2016).
- ¹⁶L. Liu *et al.*, "Terahertz focusing of multiple wavelengths by graphene metasurfaces," *Appl. Phys. Lett.* **108**, 031106 (2016).
- ¹⁷S. H. Lee, J. Choi, H. D. Kim, H. Choi, and B. Min, "Ultrafast refractive index control of a terahertz graphene metamaterial," *Sci. Rep.* **3**, 2135 (2013).
- ¹⁸H.-R. Park *et al.*, "Colossal absorption of molecules inside single terahertz nanoantennas," *Nano Lett.* **13**, 1782–1786 (2013).
- ¹⁹S. J. Park *et al.*, "Detection of microorganisms using terahertz metamaterials," *Sci. Rep.* **4**, 4988 (2014).
- ²⁰Y. Todorov *et al.*, "Strong light-matter coupling in subwavelength metal-dielectric microcavities at terahertz frequencies," *Phys. Rev. Lett.* **102**, 186402 (2009).
- ²¹G. Scalari *et al.*, "Ultrastrong coupling of the cyclotron transition of a 2D electron gas to a THz metamaterial," *Science* **335**, 1323–1326 (2012).
- ²²R. Singh, C. Rockstuhl, and W. Zhang, "Strong influence of packing density in terahertz metamaterials," *Appl. Phys. Lett.* **97**, 241108 (2010).
- ²³J. Wallauer, A. Bitzer, S. Waselikowski, and M. Walther, "Near-field signature of electromagnetic coupling in metamaterial arrays: A terahertz microscopy study," *Opt. Express* **19**, 17283–17292 (2011).
- ²⁴J. Keller *et al.*, "Coupling surface plasmon polariton modes to complementary THz metasurfaces tuned by inter meta-atom distance," *Adv. Opt. Mater.* **5**, 1600884 (2017).
- ²⁵P.-C. Li and E. T. Yu, "Flexible, low-loss, large-area, wide-angle, wavelength-selective plasmonic multilayer metasurface," *J. Appl. Phys.* **114**, 133104 (2013).
- ²⁶P. Alonso-González *et al.*, "Experimental verification of the spectral shift between near- and far-field peak intensities of plasmonic infrared nanoantennas," *Phys. Rev. Lett.* **110**, 203902 (2013).
- ²⁷A. Bhattacharya *et al.*, "Large near-to-far field spectral shifts for terahertz resonances," *Phys. Rev. B* **93**, 035438 (2016).
- ²⁸A. Bhattacharya and J. Gómez Rivas, "Full vectorial mapping of the complex electric near-fields of THz resonators," *APL Photonics* **1**, 086103 (2016).
- ²⁹F. Blanchard, K. Ooi, T. Tanaka, A. Doi, and K. Tanaka, "Terahertz spectroscopy of the reactive and radiative near-field zones of split ring resonator," *Opt. Express* **20**, 19395–19403 (2012).
- ³⁰A. Bitzer, A. Ortner, H. Merbold, T. Feurer, and M. Walther, "Terahertz near-field microscopy of complementary planar metamaterials: Babinet's principle," *Opt. Express* **19**, 2537–2545 (2011).
- ³¹O. Mitrofanov *et al.*, "Near-field spectroscopy and imaging of subwavelength plasmonic terahertz resonators," *IEEE Trans. Terahertz Sci. Technol.* **6**, 382–388 (2016).
- ³²O. Mitrofanov *et al.*, "Detection of internal fields in double-metal terahertz resonators," *Appl. Phys. Lett.* **110**, 061109 (2017).
- ³³A. J. Huber, F. Keilmann, J. Wittborn, J. Aizpurua, and R. Hillenbrand, "Terahertz near-field nanoscopy of mobile carriers in single semiconductor nanodevices," *Nano Lett.* **8**, 3766–3770 (2008).
- ³⁴J. Dorfmueller *et al.*, "Fabry-Pérot resonances in one-dimensional plasmonic nanostructures," *Nano Lett.* **9**, 2372–2377 (2009).
- ³⁵M. M. Wiecha *et al.*, "Direct near-field observation of surface plasmon polaritons on silver nanowires," *ACS Omega* **4**, 21962–21966 (2019).
- ³⁶J. Chen *et al.*, "Optical nano-imaging of gate-tunable graphene plasmons," *Nature* **487**, 77 (2012).
- ³⁷F. Hu *et al.*, "Imaging the localized plasmon resonance modes in graphene nanoribbons," *Nano Lett.* **17**, 5423–5428 (2017).
- ³⁸Z. Fei *et al.*, "Gate-tuning of graphene plasmons revealed by infrared nano-imaging," *Nature* **487**, 82 (2012).
- ³⁹P. Dean *et al.*, "Apertureless near-field terahertz imaging using the self-mixing effect in a quantum cascade laser," *Appl. Phys. Lett.* **108**, 091113 (2016).
- ⁴⁰J. Keeley *et al.*, "Detection sensitivity of laser feedback interferometry using a terahertz quantum cascade laser," *Opt. Lett.* **44**, 3314–3317 (2019).
- ⁴¹R. Degl'Innocenti *et al.*, "Terahertz nanoscopy of plasmonic resonances with a quantum cascade laser," *ACS Photonics* **4**, 2150–2157 (2017).
- ⁴²A. D. Rakić *et al.*, "Swept-frequency feedback interferometry using terahertz frequency QCLs: A method for imaging and materials analysis," *Opt. Express* **21**, 022194 (2013).
- ⁴³M. C. Giordano *et al.*, "Phase-resolved terahertz self-detection near-field microscopy," *Opt. Express* **26**, 18423–18435 (2018).
- ⁴⁴P. Di Pietro *et al.*, "Observation of Dirac plasmons in a topological insulator," *Nat. Nanotechnol.* **8**, 556–560 (2013).
- ⁴⁵P. Alonso-González *et al.*, "Acoustic terahertz graphene plasmons revealed by photocurrent nanoscopy," *Nat. Nanotechnol.* **12**, 31–35 (2017).
- ⁴⁶B. Knoll and F. Keilmann, "Near-field probing of vibrational absorption for chemical microscopy," *Nature* **399**, 134–137 (1999).
- ⁴⁷B. Knoll and F. Keilmann, "Enhanced dielectric contrast in scattering-type scanning near-field optical microscopy," *Opt. Commun.* **182**, 321–328 (2000).
- ⁴⁸B. Deutsch, R. Hillenbrand, and L. Novotny, "Near-field amplitude and phase recovery using phase-shifting interferometry," *Opt. Express* **16**, 494 (2008).
- ⁴⁹A. S. McLeod *et al.*, "Model for quantitative tip-enhanced spectroscopy and the extraction of nanoscale-resolved optical constants," *Phys. Rev. B* **90**, 085136 (2014).
- ⁵⁰P. Dean *et al.*, "Terahertz imaging through self-mixing in a quantum cascade laser," *Opt. Lett.* **36**, 2587–2589 (2011).
- ⁵¹B. Hecht, H. Bielefeldt, Y. Inouye, D. W. Pohl, and L. Novotny, "Facts and artifacts in near-field optical microscopy," *J. Appl. Phys.* **81**, 2492–2498 (1997).
- ⁵²V. E. Babicheva, S. Gamage, M. I. Stockman, and Y. Abate, "Near-field edge fringes at sharp material boundaries," *Opt. Express* **25**, 23935–23944 (2017).
- ⁵³S. Mastel *et al.*, "Understanding the image contrast of material boundaries in IR nanoscopy reaching 5 nm spatial resolution," *ACS Photonics* **5**, 3372–3378 (2018).
- ⁵⁴N. Ocelic, A. Huber, and R. Hillenbrand, "Pseudoheterodyne detection for background-free near-field spectroscopy," *Appl. Phys. Lett.* **89**, 101124 (2006).
- ⁵⁵T. Taimre *et al.*, "Laser feedback interferometry: A tutorial on the self-mixing effect for coherent sensing," *Adv. Opt. Photonics* **7**, 570–631 (2015).
- ⁵⁶A. D. Rakić *et al.*, "Sensing and imaging using laser feedback interferometry with quantum cascade lasers," *Appl. Phys. Rev.* **6**, 021320 (2019).
- ⁵⁷P. Janassek, S. Hartmann, A. Molitor, F. Michel, and W. Elsaßer, "Investigations of the polarization behavior of quantum cascade lasers by Stokes parameters," *Opt. Lett.* **41**, 305 (2016).
- ⁵⁸D. Dhirhe, T. J. Slight, B. M. Holmes, and C. N. Ironside, "Active polarisation control of a quantum cascade laser using tuneable birefringence in waveguides," *Opt. Express* **21**, 024267 (2013).
- ⁵⁹A. Cvitkovic, N. Ocelic, and R. Hillenbrand, "Analytical model for quantitative prediction of material contrasts in scattering-type near-field optical microscopy," *Opt. Express* **15**, 8550–8565 (2007).
- ⁶⁰P. Rubino *et al.*, "All-electronic phase-resolved THz microscopy using the self-mixing effect in a semiconductor laser," *ACS Photonics* **8**, 1001–1006 (2021).
- ⁶¹J. Keeley *et al.*, "Three-dimensional terahertz imaging using swept-frequency feedback interferometry with a quantum cascade laser," *Opt. Lett.* **40**, 994 (2015).
- ⁶²D. R. Bacon *et al.*, "Free-space terahertz radiation from a LT-GaAs-on-quartz large-area photoconductive emitter," *Opt. Express* **24**, 26986–26997 (2016).
- ⁶³B. Schaefer, E. Collett, R. Smyth, D. Barrett, and B. Fraher, "Measuring the Stokes polarization parameters," *Am. J. Phys.* **75**, 163–168 (2007).